The Dynamics of Megafire Smoke Plumes in Climate Models: Why a Converged Solution Matters for Physical Interpretations

S.R. Guimond[1], J. Reisner[2], and M. Dubey[2]

[1]Joint Center for Earth Systems Technology and Department of Physics, University of Maryland Baltimore County, Baltimore, MD, USA
[2]Los Alamos National Laboratory, Los Alamos, NM, USA

Key Points:

- Simulations of megafire smoke plumes require fully resolved dynamics ($\sim 8\ \Delta x$) in order to accurately characterize plume properties (e.g., black carbon fraction)
- For the 2017 British Columbia event, smoke injected at $\sim$ 12 km height requires a reduction in black carbon fraction by 50% to match observations for external mixtures
- Analysis of the vorticity dynamics shows that smoke plume anti-cyclonic vortices form (decay) due to the dilution (concentration) of cyclonic absolute vorticity

Corresponding author: Stephen R. Guimond, `sguimond@umbc.edu`

Abstract

As the climate system warms, megafires have become more frequent with devastating effects. A byproduct of these events is the creation of smoke plumes that can rise into the stratosphere and spread across the globe where they reside for many months. To gain a deeper understanding of the plume dynamics, global climate simulations of a megafire were performed at a wide range of grid spacings from 2.0° down to 7 km, including a 7 km nonhydrostatic experiment. The analysis focuses on how the resolved dynamics affects the specification of the plume characteristics such as injection height and black carbon (BC) mass. Prior studies initialize the smoke plume at one or a few grid points and this is shown here to produce severely dissipative dynamics. In order to validate such simulations with observations, enhancements of the plume characteristics to offset the dissipation is necessary. Using a numerically converged simulation, sensitivity tests show that to approximate the observed stratospheric lifetime, a reduction in BC fraction by 50% is necessary for external mixtures. The vorticity dynamics of the plume is also analyzed with a Lagrangian budget to understand the mechanisms responsible for the evolution of a collocated anticyclonic vortex. The results can be distilled down into a simple conceptual model. As the plume rises, the air diverges at the top of the updraft where the largest concentrations of smoke are found. This divergence induces a dilution of the background cyclonic absolute vorticity producing an anticyclonic vortex. Vortex decay occurs from opposite arguments.

Plain Language Summary

Recently, there has been an increase in large and intense wildfires ("megafires") across the Earth in response to global warming. These megafire events produce large amounts of smoke that can rise high up in the atmosphere to a level well above clouds and weather. The smoke can stay at these high levels for long periods of time and spread across much of the Earth, which blocks sunlight from reaching the surface. It is important to understand the properties of these smoke plumes and how to correctly predict their consequences on human life. However, uncertainties in both observations and models make it difficult to achieve these goals. In particular, models contain various sources of uncertainty that can interact in complex ways. In this paper, we show that previous research has used a model grid spacing that does not sample the plume accurately, which leads to errors that affect the interpretation of the smoke properties, evolution of the plume and potential climatic effects. By choosing a model grid spacing that accurately samples the plume structure, the errors in the dynamics component of the model can be minimized, providing a baseline for reducing uncertainty in other parts of the system.

1 Introduction

In the last several years, there has been a dramatic increase in large, intense wildfires ("megafires") in various regions of the world that have burned millions of acres of forests, destroyed homes and businesses and resulted in substantial deaths (e.g., Jolly et al., 2015; Wikipedia contributors, 2022). The production of smoke from these fires can be rapidly transported deep into the stratosphere through a combination of pyrocumulonimbus (pyroCb) events and radiation-driven lift, where it can spread globally and reside for many months to years (e.g., Fromm et al., 2005; Peterson et al., 2018; Khaykin et al., 2018). Recent megafires in British Columbia (2017; BC17) and Australia (2019/2020) have produced stratospheric aerosol mass burdens between $\sim$ 0.2 - 1.0 Tg, which is equivalent to that from a moderate volcanic eruption (Peterson et al., 2021).

A natural question to ask is: what are the impacts of these stratospheric smoke plumes on climate? While some studies have estimated the radiative forcing resulting from megafires, the global mean of this forcing is usually small and sometimes of opposite sign (Christian et al., 2019; Das et al., 2021), casting doubt on their effects on the climate system. Christian et al. (2019) studied the BC17 megafire event and estimated a direct top-of-the-atmosphere (TOA) radiative forcing between +0.01 and +0.02 Wm^{-2} compared to values between -0.7 and -1.3 Wm^{-2} from the 2008 Kasatochi volcano eruption (Wang et al., 2013). However, Christian et al. (2019) did not employ a coupled climate model in their radiative forcing calculations, eliminating aerosol indirect effects, which could result in significant uncertainty. Das et al. (2021) performed coupled climate model simulations of the BC17 event and found TOA forcing of - 0.03 $\pm$ 0.01 Wm^{-2}. While the BC17 forcings are small and potentially within the noise, for larger megafires, such as the 2019/2020 Australian event, the radiative effects can be significant with TOA forcing values of - 0.31 $\pm$ 0.09 Wm^{-2} (Khaykin et al., 2020) and mean surface temperature cooling of up to -0.2 K (D'Angelo et al., 2022).

It is clear that more in-depth studies are needed to understand the potential regional and global effects of megafire smoke plumes. To provide a more comprehensive analysis of potential climatic effects, it is important to understand the mechanisms controlling the transport of smoke and to quantify characteristics of the smoke plumes such as total mass, breakdown of that mass into organic aerosol (the focus here is on organic carbon or OC) and black carbon (BC) fractions, mean particle radius, peak height and stratospheric residence time, among others. Several recent studies have analyzed specific megafire cases to achieve this understanding and they typically utilize either satellite observations alone or in combination with climate models. The focus of the present paper is on the plume and vorticity dynamics of the BC17 megafire and therefore, a brief description of this event is discussed next. However, the discussion, results and conclusions of the present paper are sufficiently general such that they are relevant to a broader scope of megafire events.

The BC17 megafire was initiated on August 12, 2017 and produced a series of five discrete pyroCbs that lasted for about a 5 h period. Lidar satellite observations indicated that smoke from the pyroCbs reached altitudes of up to $\sim$ 13 km about 8 h after the 5 h pulsing period at 1045 UTC 13 August, which is $\sim$ 1 km above the local tropopause of $\sim$ 12 km (Peterson et al., 2018). The smoke is thought to have been directly injected into the stratosphere by the pyroCbs, but there are uncertainties with this interpretation. About 33 h later at 1930 UTC 14 August, lidar observations clearly show significant smoke at heights of $\sim$ 13.5 km, illustrating the important role of radiative lofting effects (Torres et al., 2020). The peak height of the smoke plume was $\sim$ 22 km about three weeks after the fire initiation with elevated lidar backscatter detected for $\sim$ 4 months or more (Peterson et al., 2018; Khaykin et al., 2018). In addition, the ascent rate of the BC17 plume in the first few days was estimated at $\sim$ 2 - 3 km/day and over a three week time period averaged $\sim$ 0.5 km/day (Khaykin et al., 2018).

Initially, the smoke is confined to the cores of the pyroCbs, which have a scale on the order of 10 km. However, as the pyroCbs merge and penetrate the tropopause, their outflow coupled with the strong winds near the tropopause can spread the smoke to a large horizontal area, on the order of many thousands of square kilometers. Peterson et al. (2018) estimated a smoke area of $\sim$ 800,000 km^{-2} based on an aerosol index from satellite observations, but the area of dense smoke is much smaller than this value. Estimates of the total smoke mass produced by the BC17 megafire (0.1 - 0.3 Tg) were calculated using two methods. The first method integrates the particle mass density over the volume of smoke contained in the stratosphere using lidar data, while the second method uses observations of the total burned area, fuel consumption and smoke emissions. While reasonable estimates can be obtained, there is significant uncertainty ($\sim$ 50%) in the mean mass value of 0.2 Tg.

The breakdown of smoke emissions from megafires into BC and OC is critical for plume lofting effects because BC is a strong absorber of radiation across the solar spectrum, while OC, which dominates the total smoke mass, is a very weak absorber. The associated heating of the plume from these radiative effects can loft the smoke high into the stratosphere (Malone et al., 1985). Unfortunately, there is also significant uncertainty in the BC fraction in the range of ∼ 2 - 6 % as described below. In addition, the microphysical aspects of smoke particle evolution are highly uncertain and they are treated simply in climate models. The microphysical aspects include mixing processes with other aerosols and phases of water as well as interactions with radiation (optical properties), which are complex, variable and difficult to measure.

Yu et al. (2019) used the Community Earth System Model (CESM) at 1.9° x 2.5° horizontal resolution and 56 vertical levels (∼ 1 km resolution near the tropopause) to determine the BC content and stratospheric residence time of the BC17 smoke plume. This was done by perturbing the BC fraction over a range of values (1 - 5 %) and comparing the peak height of the simulated plume to satellite observations. The plume was initialized at 12 - 13 km height, seemingly at one grid point near the fire epicenter, with 0.3 Tg of total mass. With this setup, Yu et al. (2019) inferred that a 2 % BC fraction best matched observations. They estimated a ∼ 5 month stratospheric residence time (e-folding time) from observations and an ∼ 8 month e-folding time from the simulations with 2% BC fraction. The authors determined that in order to match the observed e-folding time, a photochemical loss of OC must be invoked.

Torres et al. (2020) used the NASA Goddard Earth Observing System (GEOS) global climate model at ∼ 55 km (∼ 0.5°) horizontal resolution and 72 vertical levels (also ∼ 1 km resolution near the tropopause) to study the BC17 event. The authors used a total smoke mass of 0.3 Tg and assumed a BC fraction of 2.5%. Independent estimates of the total smoke mass were computed and they found a range of 0.18 - 0.35 Tg, similar to Peterson et al. (2018). The smoke mass was spread evenly across a 2° x 2.5° area in the horizontal (4 - 5 grid points covering the plume) and injected uniformly between 10 - 12 km altitude, which is just below the tropopause height. The main takeaway from this study is the significant impact of radiative self-lofting in driving the plume into the stratosphere to high altitudes (up to 20 - 22 km height) with diabatic heating rates of 20 K/day or more.

Das et al. (2021) used the simulation described in Torres et al. (2020) to study additional aspects of the BC17 event, including the radiative forcing discussed above. They found a stratospheric e-folding time of 140 days (4.67 months) from their simulation after starting the calculation 38 days from the initial injection. An estimate of this timescale from a satellite retrieval was similar (5 months) although the decay rate appears slightly steeper than the model. Both Christian et al. (2019) and Das et al. (2021) do not need to include a photochemical loss of OC to approach the observed stratospheric e-folding time, casting doubt on the results presented in Yu et al. (2019).

D'Angelo et al. (2022) (hereafter D22) conducted global simulations of the BC17 event from the CESM and GEOS models to understand the sensitivity of plume peak height and stratospheric residence time to BC fraction (2 - 6 %), injection height (12 - 14 km), total mass (0.1 - 0.3 Tg) and particle radius (200 - 350 nm). The control simulations used a BC fraction of 2%, stratospheric injection height of ∼ 13.5 km and mean particle radius of 300 - 350 nm. The total injected mass was 0.4 Tg, but only 0.2 Tg was injected at ∼ 13.5 km height with the other 0.2 Tg spread evenly below this altitude. This setup mirrors that of Christian et al. (2019). The control setup produced a stratospheric e-folding time of ∼ 5 months for the CESM model and ∼ 6 months for the GEOS model.

D22 found the most sensitive parameters (in order from largest to smallest) to be plume injection height, total mass/BC fraction (together determine BC load) and particle radius. These parameters are not only sensitive in models, but they have significant uncertainty from measurements as described above. The particle sizes, however, have minimal sensitivity for a reasonable measurement range. The plume injection height is a consequence of the typically very coarse resolution of climate models, which cannot resolve the natural life cycle of pyroCbs in any form. As a result, the altitude that convection transports smoke into the upper atmosphere must be specified to initialize the model. For the BC17 case, measurements of this altitude are uncertain with values ranging from $\sim$ 11 - 14 km.

There is another source of uncertainty that has not been addressed methodically with megafire studies: the effects of resolved energetics in the climate models and feedbacks to the uncertainties associated with the plume characteristics. Most of the modeling studies are conducted with very coarse grid spacing (e.g., 1° - 2°) with the plume initialized at one grid point, although Torres et al. (2020) and Das et al. (2021) used 0.5° covering the plume with 4 - 5 grid points. What are the effects of higher resolution on the smoke plume dynamics (e.g., transport, large-scale mixing and interactions with clouds) and interplay with the specified plume characteristics (e.g., injection height, total smoke mass and BC fraction)? The purpose of this paper is to answer these questions and make recommendations to the community for a minimally resolvable modeling system that can narrow the uncertainty gap for the megafire problem.

The remainder of the paper is organized as follows. In Section 2, a description of the numerical model and setup of the simulations is presented. Simulations are conducted at a wide range of resolutions to study the effects of resolved dynamics: 2.0°, 1.0°, 0.25°, 7 km and 7 km-nonhydrostatic. Analysis of the characteristics and transport of the simulated smoke plumes is described in Section 3. Section 3 also presents an analysis of the kinetic energy spectra of the simulations and discusses the effective resolution of the GEOS modeling system. Section 4 presents an analysis of the vorticity dynamics of the plumes and how this relates to the plume lifetime. Important implications of this work for the megafire problem are given in Section 5. Future work is also discussed in this section.

2 Numerical Simulations

2.1 Description and setup of climate model

To examine the global effects of localized megafire smoke plumes, numerical simulations of the BC17 event were conducted with the atmospheric component of the NASA GEOS climate model. The NASA GEOS is a finite volume general circulation model that solves the hydrostatic or nonhydrostatic equations of motion on a cubed sphere grid with a Lagrangian vertical coordinate (Lin, 2004). The dynamic core is coupled to various physical models for moist processes, radiation, turbulence, gravity wave drag, etc. (Molod et al., 2015) and is initialized with reanalysis data that incorporates various observations (MERRA-2) (Rienecker et al., 2008). In this study, the Goddard Chemistry, Aerosol, Radiation and Transport (GOCART) (Chin et al., 2002) model is utilized to represent smoke plumes with a focus on the bins for BC and OC aerosol. The aerosols in GOCART are treated as an external mixture and are fully coupled to the dynamic core and radiation packages. The source of BC/OC for the BC17 event is described below and the sinks include wet scavenging and dry deposition. Given the focus on the stratosphere, the dry deposition processes are most important. This dry deposition is a parameterization of gravitational settling based on particle size and air viscosity (Chin et al., 2002). Also note that no interactive chemistry model is employed in the simulations. These simplifications reduce the degrees of freedom in the simulations and places the focus of the analysis on the dynamics of the problem.

Simulations with GEOS are conducted with a wide range of uniform horizontal grid spacings across the globe: 2.0°, 1.0°, 0.25° and 7 km. The vertical grid for all simulations was set to 72 hybrid sigma-pressure vertical layers from the surface to the model top at 0.01 hPa. Utilization of the same vertical grid for all simulations enables a direct comparison of the resolved energetics of each simulation. The vertical grid spacing is $\sim$ 1 km where the smoke plume is initialized in the stratosphere. These simulations are all run with hydrostatic dynamics, but an additional run at 7 km is conducted with nonhydrostatic dynamics to examine the effects of the vertical inertial terms (advection of vertical velocity plus the local time tendency), as well as a diffusion term, on the plume heights and stratospheric residence time of the smoke. In general, nonhydrostatic effects become more important for scales of $\sim$ 10 km and below (e.g., Weisman et al., 1997). Also, note that the GEOS model is run in a "free" mode without observational nudging and in this sense represents a true predictive simulation. The MERRA-2 reanalysis fields are used as initial conditions for the simulations and the model is started at 2100 UTC 9 August 2017, which is about three days prior to the injection of smoke. This allows the model to spin-up for a period of time and develop a more robust energy spectrum.

The BC17 plume is represented in the model by injecting smoke mass following the specification outlined in Christian et al. (2019) and D22 due to the simplicity and ability to compare with prior work. For the 2.0° simulation, the smoke mass is initialized at a single grid point (close to 53.5°N,123.0°W; an approximate epicenter for the BC17 plume) with 0.2 Tg injected at $\sim$ 13.5 km height in the stratosphere and 0.2 Tg spread evenly in the troposphere. Of the total mass, 98% is specified as OC and 2% as BC following the results of Yu et al. (2019) and D22. This smoke profile is held fixed in the model for a 5 h time period starting at 1900 UTC 12 August 2017. A mean particle radius of 350 nm is used for all simulations. Similarities and differences of the smoke plume initialization described here with that from prior work can be found in the introduction section.

The setup of the simulations at the other grid spacings is identical to that described above except the smoke mass is spread evenly across the higher resolution grids to match the 2.0° grid cell area. For example, the smoke mass is spread evenly across 4 grid points (2 in each horizontal dimension) for the 1.0° simulation, 64 grid points for the 0.25° and 1024 grid points for the 7 km runs in the same location as the 2.0° cell. Integration of the total smoke mass on the native cubed sphere grid showed nearly identical values across all simulations indicating a consistent set of initial forcing with uniform smoke concentration. For post-processing, all model output is interpolated to a regularly spaced latitude/longitude grid that matches the listed simulation resolution.

3 Characteristics of Plume Evolution

3.1 Stratospheric Lifetime and Smoke Structure

To summarize the smoke plume evolution in the simulations, a time series of the globally integrated stratospheric smoke burden at a wide range of horizontal grid spacings is presented in Fig. 1. In this analysis, the stratosphere is loosely defined as heights above 150 hPa or $\sim$ 12.5 km in the region where the plume is present. All simulations are run up until the plume stratospheric lifetime, which is defined as where the peak stratospheric mass (sampled at $\sim$ 6 days into the simulations) falls off to $1/e$, using the globally integrated values shown in Fig. 1. In Fig. 1 and all other figures shown in this paper, time refers to the number of days after the start of the plume forcing (1900 UTC 12 August 2017).

Figure 1 shows that the 2.0° simulation falls off very rapidly with a lifetime of 3.5 months, followed by the 1.0° simulation at 5.9 months, 7 km nonhydrostatic at 6.8 months, 7 km at 6.9 months and 0.25° at 7.2 months. Using the 7 km simulation as the high resolution reference to evaluate the other hydrostatic runs, the 2.0° and 1.0° simulations significantly underestimate the stratospheric lifetime by $\sim$ 50% and 15%, respectively, while the 0.25° simulation only slightly overestimates the lifetime by $\sim$ 4%. The 7 km nonhydrostatic lifetime is slightly less than the corresponding 7 km hydrostatic value, which indicates that nonhydrostatic dynamics (including the vertical inertial term as well as

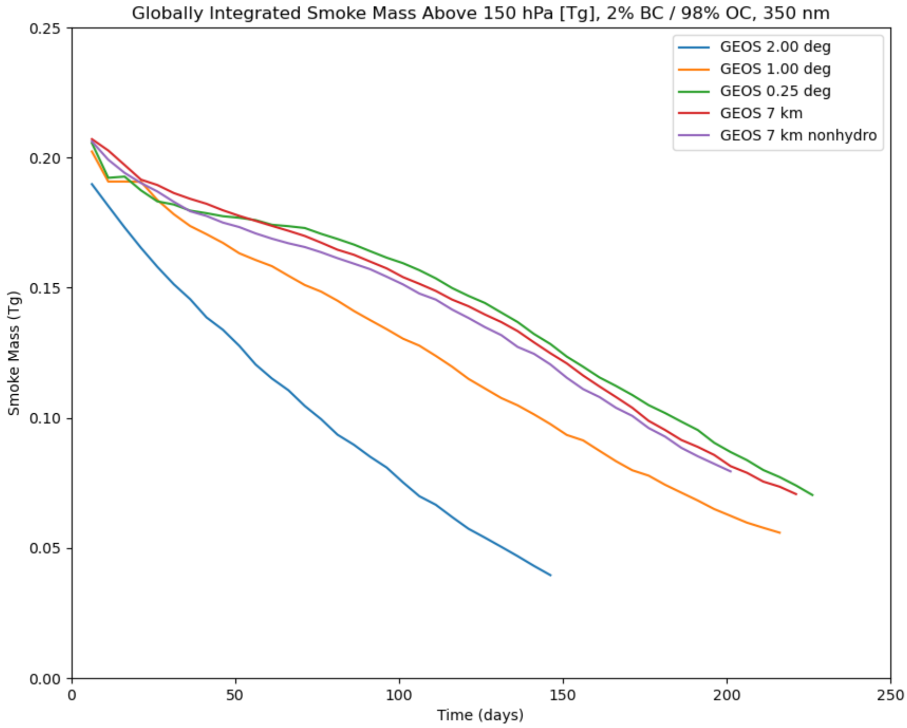

Figure 1: Time series of the globally integrated stratospheric (above 150 hPa) smoke burden in Tg for simulations at a wide range of horizontal grid spacings.

a diffusion term) are contributing an overall dissipative effect on the plume lofting and stratospheric lifetime. Even finer grid spacing than 7 km will likely lead to additional small differences, but such simulations are an enormous computational burden and are left for future work.

Figure 1 also shows there is some variability in the individual curves, with the exception of the 2.0° simulation, at time periods less than about 30 - 50 days due to variability in the horizontal and vertical transport of the smoke. After about 50 days, the curves become smooth, which is consistent with the slow and steady removal of smoke from the stratosphere by sedimentation. It is difficult to estimate the stratospheric lifetime from observations due to smoke plume detection issues (limited sampling in space and time, signal-to-noise ratio of instrument, etc), but studies have indicated that ~ 5 months is a reasonable value (Peterson et al., 2018; Khaykin et al., 2018; Yu et al., 2019; Das et al., 2021). However, in this section, we are not as concerned with the absolute truth of the simulations, which are only quasi-realistic representations of the BC17 event. For example, there are various unknown and uncertain factors surrounding the plume characteristics as described in the introduction. Instead, we are focused on studying the relative truth of the simulations and the reasons for the wide range of variability presented in Fig. 1 that can guide more focused case studies of the BC17 event or other megafire cases.

The stratospheric lifetime discussed above is directly related to the peak height the plume reaches in each simulation. Figure 2 shows the zonal mean smoke mixing ratio

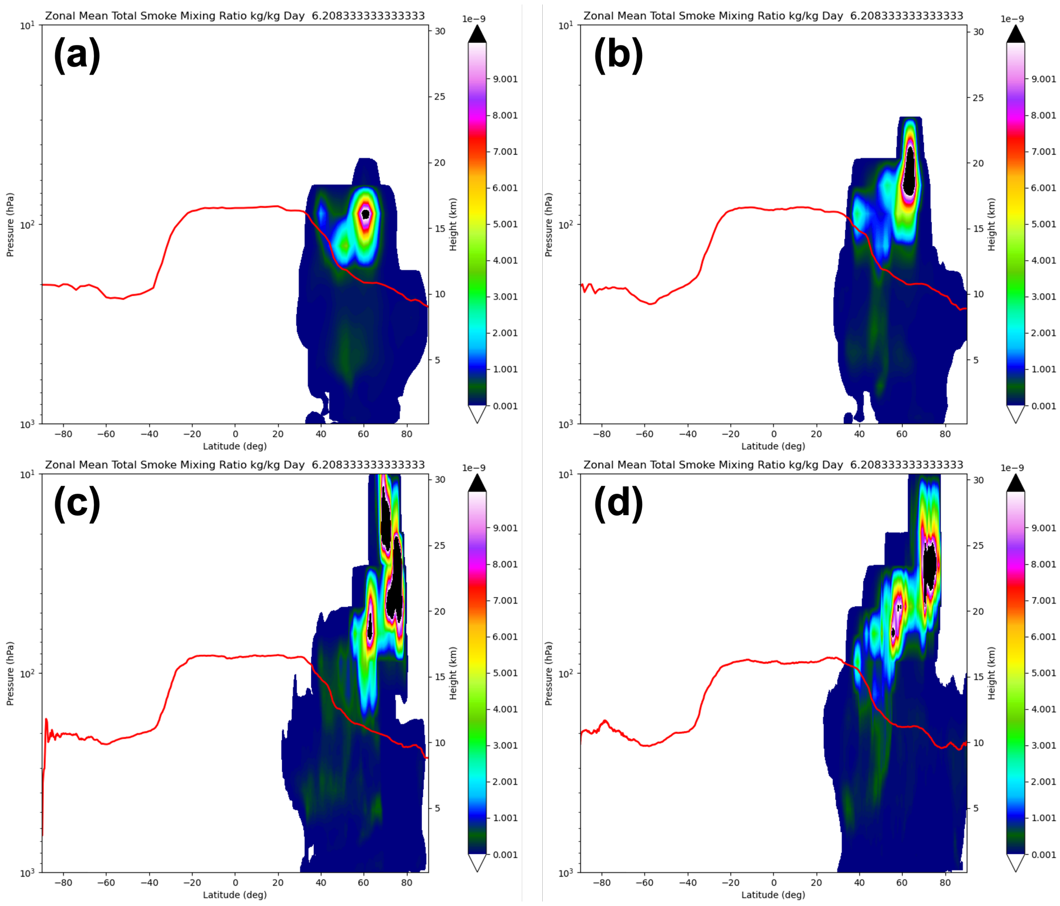

Figure 2: Zonal mean total smoke mixing ratio in kg/kg at 6.2 days into the simulations for varying resolutions, (a) 2.0° (b) 1.0° (c) 0.25° and (d) 7 km. The red line shows the tropopause height.

as a function of latitude and height at 6.2 days into the simulations. The peak height of the plume, defined qualitatively as the leading edge of the large smoke mixing ratio core, varies widely with resolution. The peak height values are ∼ 18 km, 23 km, 32 km and 30 km in the 2.0°, 1.0°, 0.25° and 7 km simulations, respectively. Relative to the 7 km reference simulation, the 2.0° and 1.0° simulations drastically underestimate the peak height by 40% and 23%, respectively, while the 0.25° simulation slightly overestimates the peak height by about 6%. The 2.0° and 1.0° simulations have one primary smoke core that is concentrated near 60° latitude, while the 0.25° and 7 km simulations have two cores with one near 60° latitude and the other closer to 70° latitude. The two smoke cores are more distinct in the 7 km simulation. The vast majority of the smoke is above the tropopause at this time in all simulations, but the dense smoke is closer to this boundary in the 2.0°and 1.0° simulations.

At 16.2 days into the simulations, shown in Fig. 3, the peak height of the plumes are ∼ 19 km, 30 km, 38 km and 35 km in the 2.0°, 1.0°, 0.25° and 7 km simulations, respectively. The 2.0° and 1.0° simulations underestimate the peak height by ∼ 46% and 14%, respectively, while the 0.25° simulation slightly overestimates this height by ∼ 8%. The rise rate of the 1.0° simulation is largest at 0.7 km/day, followed by the 0.25° (0.6 km/day), 7 km (0.5 km/day) and 2.0° (0.1 km/day). Most of the plumes are concentrated into one column with the exception of the 7 km run, which continues to display two main

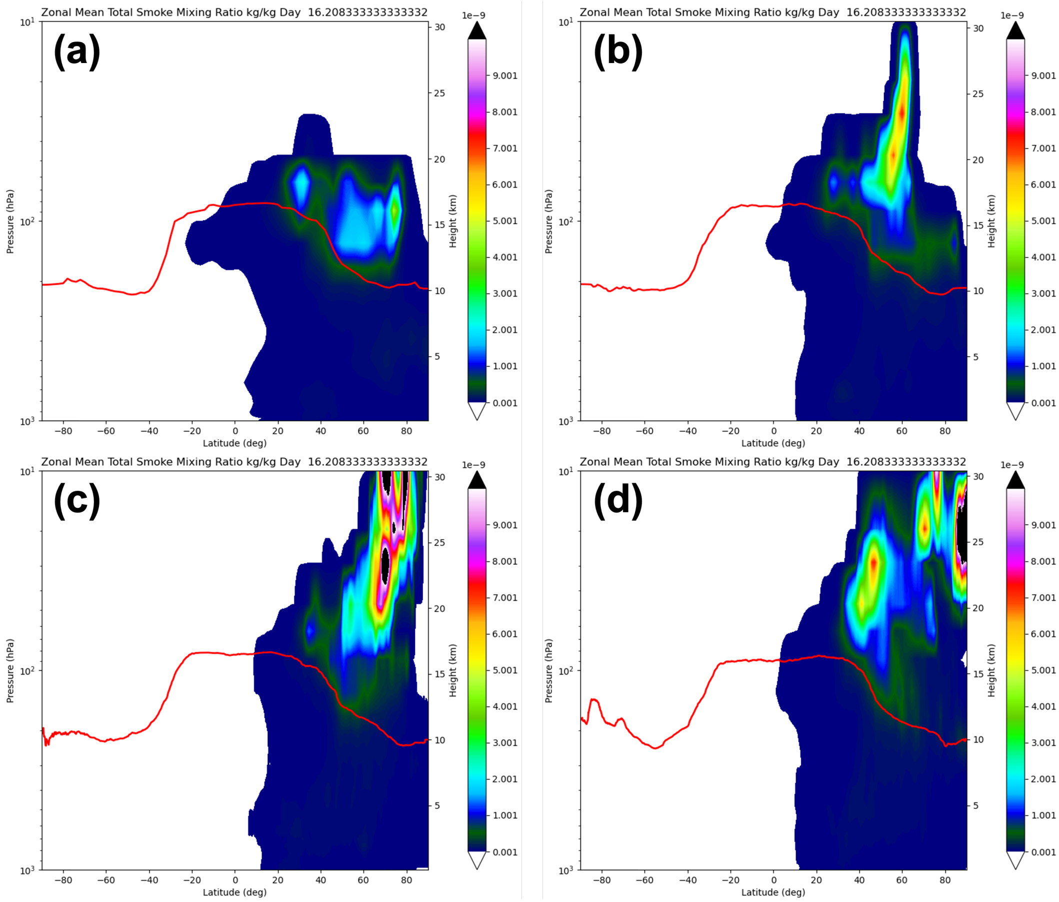

Figure 3: The same as in Fig. 2, only at 16.2 days.

cores with one centered at ∼ 45° latitude and 23 km height and the other at ∼ 80° latitude and 26 km height. Nearly all the smoke is above the tropopause at this time period, but the 2.0° simulation (Fig. 3a) shows large concentrations sitting very close to the edge of the boundary. Note that the peak height of the plumes over time are found at ∼ 20 - 25 days into the simulations with values not much larger than that described here at 16.2 days.

The vertical transport of the plumes observed in Figs. 2 and 3 is due to the self-lofting effect described in the introduction whereby BC absorbs solar radiation and forms a heating anomaly, which causes a buoyant updraft. The large variability in the solutions with grid spacing, which all have the same plume initialization and model setup, is due to the effects of resolved energetics in the model. Detailed examination of this effect will be presented in section 3.2.

Figure 4 shows the horizontal structure of the smoke plume at 6.2 days by vertically integrating the total smoke mixing ratio over the entire model atmosphere. At this time period, the 2.0° run (Fig. 4a) shows a single ball of smoke located over the Hudson Bay in Canada with a long tail of elevated concentrations extending across the Atlantic Ocean and into Western Europe. The other resolution simulations have similar placement of the large-scale features, but the single ball of smoke in the 2.0° run is broken down into increasingly smaller-scale structures that move smoke further outward from the core region. For example, in the 1.0° (Fig. 4b), 0.25° (Fig. 4c) and 7 km (Fig. 4d)

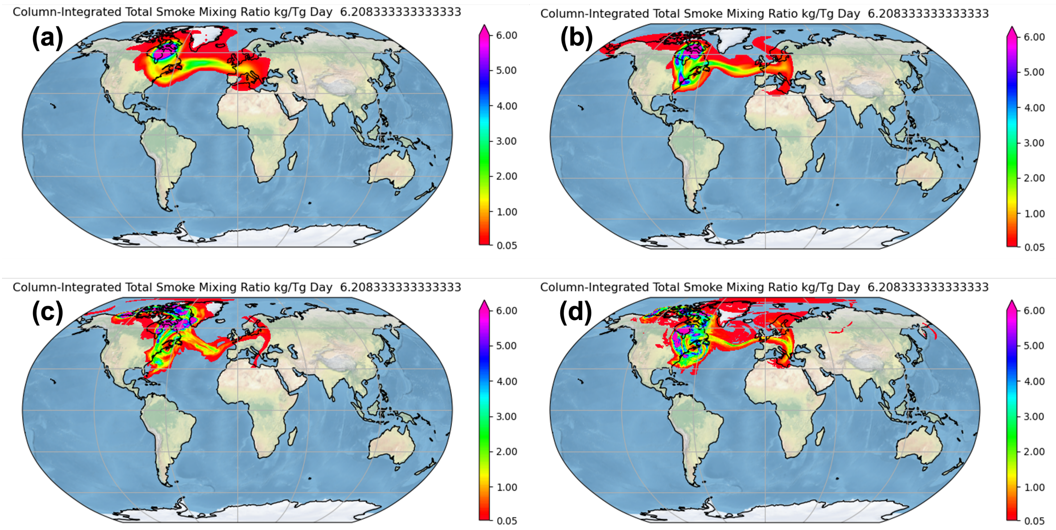

Figure 4: Vertically integrated total smoke mixing ratio in kg/Tg over the entire model atmosphere at 6.2 days into the simulations for varying resolutions, (a) 2.0° (b) 1.0° (c) 0.25° and (d) 7 km.

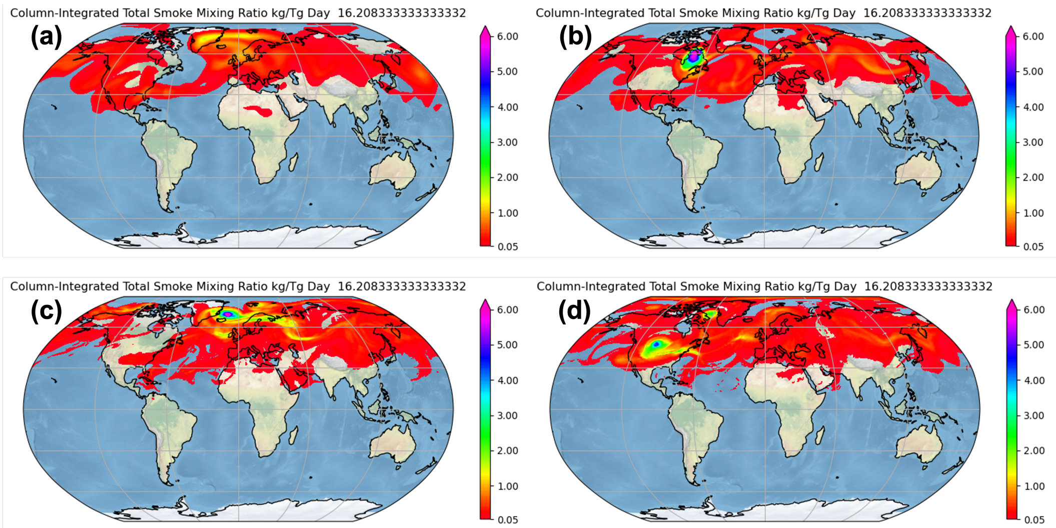

Figure 5: The same as in Fig. 4, only at 16.2 days.

simulations, high concentrations of smoke are found in the Southeastern United States and in the 0.25° and 7 km runs more smoke has moved North and West into far Northern Canada near the Beaufort Sea. The main location of the smoke plume over Northeastern Canada (near Hudson Bay) depicted in the modeling results are in general agreement with satellite observations close to this time period ($\sim$ 19 August, 2017) (Khaykin et al., 2018).

At 16.2 days (Fig. 5), the horizontal structure of the smoke plume is significantly different between the various resolution simulations. In the 2.0° run (Fig. 5a) the highest smoke concentrations are no longer organized into a coherent, circular structure but instead are stretched and diffused over the Greenland region. The other resolution simulations display a concentrated, circular structure with peak smoke mixing ratio values at the center. In the 1.0° run (Fig. 5b) this structure is located over Eastern Canada while in the 0.25° run (Fig. 5c) the ball of smoke is centered just off of Greenland. In the 7 km run (Fig. 5d), two circular regions of smoke exist with the larger feature located over the Northern Great Plains of the United States and the smaller feature located just to the West of Greenland. Lower values of smoke mixing ratio are scattered North of 30° N latitude in roughly similar locations in all simulations.

Satellite observations close to this time period ($\sim$ 29 August, 2017) (Khaykin et al., 2018) indicate that the smoke plume has encircled the globe and is located back near Western Canada, which is in closer agreement with the 7 km resolution simulation. However, at this stage of the paper, we are only establishing relative truth between the simulations and their variability, with the 7 km hydrostatic run serving as the high resolution reference. The horizontal structure differences between the various resolution simulations at this time is due to the differing heights of the plumes and associated wind fields that drive the transport at those heights as well as the nonlinear evolution. The nonlinear evolution is dependent on the resolved energetics of each simulation and will cause greater divergence among the simulation members as time moves forward. This is partly why the smoke horizontal structure at 6.2 days is in much better agreement than that shown at 16.2 days.

3.2 Kinetic Energy Spectra

The previous section demonstrated large variability in the stratospheric lifetime and smoke structure as a function of model grid spacing for the exact same parameters defining the initialized smoke plume. The main source of this variability is the resolved energetics of the GEOS modeling system and the associated sampling of the initialized smoke plume. To demonstrate this point, spectral analysis of the model data is performed.

The discrete Fourier transform (DFT) of a variable Ψ in one spatial dimension λ on a periodic domain with constant grid spacing can be written

$$\Psi(\lambda_n) = \sum_{m=-Q}^{Q} F(k_m) e^{ik_m\lambda_n} = F(0) + 2\left|\sum_{m=1}^{Q} F(k_m) e^{ik_m\lambda_n}\right| \tag{1}$$

where $\lambda_n = L(n-1)/N$ is the position along the λ dimension for index n over domain length L with N grid points, $k_m = 2\pi m/L$ is the wavenumber for index m, and Q represents the highest wavenumber index on the grid (length scale of two times the grid spacing). The complex Fourier coefficients are given by

$$F(k_m) = N^{-1} \sum_{n=1}^{N} \Psi(\lambda_n) e^{-ik_m\lambda_n}. \tag{2}$$

In the calculation of the DFT, it is common practice to report on the positive wavenumbers only, which requires multiplying wavenumbers larger than zero by a factor of two to account for the removal of the negative side of the spectrum. For each model simulation, the DFT is computed for each horizontal velocity component along the λ direction (latitude) according to the equations above and the kinetic energy spectrum per unit mass is calculated,

$$E(k) = \frac{\hat{u}^2 + \hat{v}^2}{2} \tag{3}$$

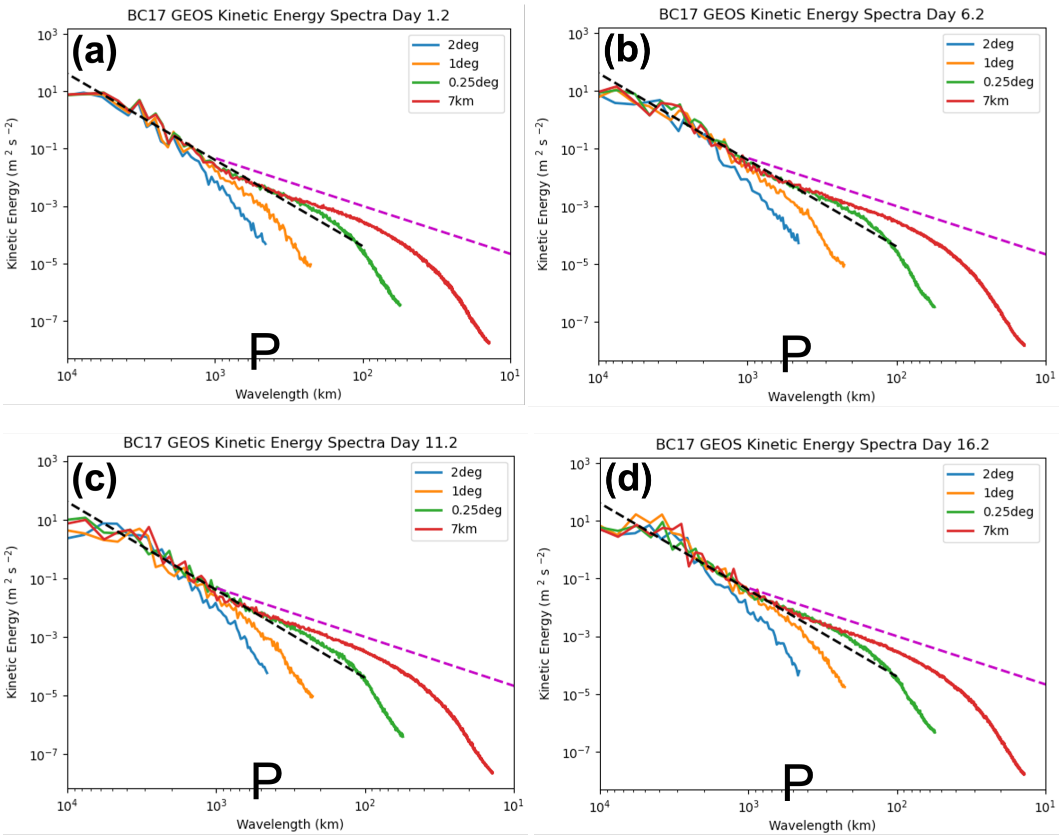

Figure 6: Horizontal kinetic energy spectra (m^2/s^2) averaged over the 40° – 70°N latitude band and 150 – 10 hPa in height at various resolutions in GEOS for (a) 1.2 days, (b) 6.2 days, (c) 11.2 days and (d) 16.2 days into the simulations. The dashed black and purple lines denote the -3 and -5/3 spectral slopes of large-scale and mesoscale kinetic energy, respectively, from theory and observations. The "P" letter marks the scale of the initial smoke plume forcing.

where the hat over the velocity variables denotes the DFT field. The kinetic energy spectrum is then averaged over the 40°N - 70°N latitudinal band and the 150 - 10 hPa layer where the smoke plume activity is largest.

Figure 6 shows the mean horizontal kinetic energy spectra for the various resolution simulations at early time periods (t $\leq \sim$ 16 days) in the simulations when much of the lofting dynamics takes place. At all time periods shown in Fig. 6, the kinetic energy is significantly damped in the 2.0° and 1.0° simulations (especially the 2.0° run) relative to the 0.25° and 7 km simulations from scales of $\sim$ 200 km - 1000 km. Most of the plume dynamics is occurring within this wavelength band given that the scale of the initial disturbance is $\sim$ 500 km (marked in Fig. 6), which is near the minimum resolvable wavelength of the 2.0° simulation (2 Δx, where Δx is the approximate grid spacing of the simulations). The 0.25° simulation spectra are very similar to the 7 km simulation spectra in the $\sim$ 200 km - 1000 km wavelength band, which indicates that the 0.25° simulation is nearly converged for the majority of the plume dynamics. This result is consistent with the statistics presented in section 3.1, where the 0.25° run produced small errors relative to the 7 km reference simulation. Furthermore, Fig. 6 illustrates that only the 0.25° and 7 km simulations match the slopes of kinetic energy from theory and observations (e.g., Nastrom & Gage, 1985). In the $\sim$ 200 km - 1000 km wavelength band, the 0.25°

and 7 km simulations tend to follow a -3 spectral slope ("large scales") at 1.2 and 6.2 days (Figs. 6a and b, respectively), but evolve a bit closer to a -5/3 slope ("mesoscales") at 11.2 and 16.2 days (Figs. 6c and d, respectively). This shift is subtle and not overly significant given that there is an overlap in the observed spectral slopes in this wavelength band.

Figure 6 also shows the 0.25° simulation has damped kinetic energy relative to the 7 km run from scales of $\sim$ 50 km - 300 km, including some subtle temporal variability in the spectra. The wavelength where the 0.25° run begins to dissipate kinetic energy relative to the 7 km run narrows from $\sim$ 300 km wavelength (Figs. 6a,b,c) down to $\sim$ 200 km wavelength (Fig. 6d). These results indicate that the effective resolution of the GEOS modeling system is $\sim$ 7 - 8 Δx, which is similar to other global modeling systems (e.g., Skamarock et al., 2014). *Thus, in order to produce a dynamically accurate and well-resolved simulation, the smoke plume must be sampled by the model grid with $\sim$ 8 grid points, which should produce the correct slope of kinetic energy as demonstrated in Fig. 6.*

3.3 Optimal Simulations

The previous sub-section illustrated that in order to ensure a dynamically accurate evolution, the plume must be sampled by the model grid at $\sim$ 7 - 8 Δx, which results in 0.25° spacing for the initial conditions specified in this work. Given this setting for the dynamics, how should the other uncertain parameters defining the smoke plume (injection height, total smoke mass, BC fraction and particle radius) be specified to produce an optimal simulation?

Several sensitivity tests were conducted with 0.25° spacing to examine the optimal settings of these parameters relative to observations. The observations used to constrain this exercise are estimates of the stratospheric lifetime of the smoke plume ($\sim$ 5 months) (Peterson et al., 2018; Khaykin et al., 2018; Yu et al., 2019; Das et al., 2021) and to some extent peak heights ($\sim$ 22 km) (Peterson et al., 2018; Khaykin et al., 2018; Das et al., 2021).

The injection height used in the initial simulations (13.5 km) was determined to be too high based on observational estimates that placed the plumes at 11.5 - 12.5 km height with the best estimate likely at or slightly above the local tropopause height ($\sim$ 12 km) (Peterson et al., 2018). This injection height is also utilized in previous modeling studies (e.g., Yu et al., 2019). For the sensitivity tests discussed here, simulations were performed with an injection height of 11.5 km and 12.5 km, given the vertical grid spacing of the chosen model grid (1.0 km). The total column smoke mass (0.4 Tg with 0.2 Tg injected in the stratosphere) and particle radius (350 nm) were not changed. Some short (60 day) sensitivity tests that examined the impact of the 0.2 Tg of smoke spread evenly throughout the troposphere were also conducted. These tests showed that by removing the 0.2 Tg of smoke in the troposphere, the total smoke mass in the stratosphere is reduced by only $\sim$ 4%. This indicates that for the distribution of mass utilized here, the amount of smoke rising into the stratosphere from the troposphere is quite small. Thus, our focus is on the smoke injected in the stratosphere. For the 11.5 km injection height a BC mass fraction of 2% was utilized, as in the initial set of simulations, while for the 12.5 km height, BC mass fractions of 0.5%, 0.75% and 2% were performed. Table 1 summarizes the smoke plume and model resolution settings utilized for these sensitivity tests along with those for the control experiments.

Figure 7 shows the results of some of these 0.25° sensitivity tests in terms of the horizontally averaged total smoke mixing ratio. The center of mass of the smoke plume is drawn on each simulation as a measure of the plume height. It should be noted that there are uncertainties comparing this height to observations, such as from lidar, due to the difficulties in simulating the penetration depth of the instrument signal into the smoke

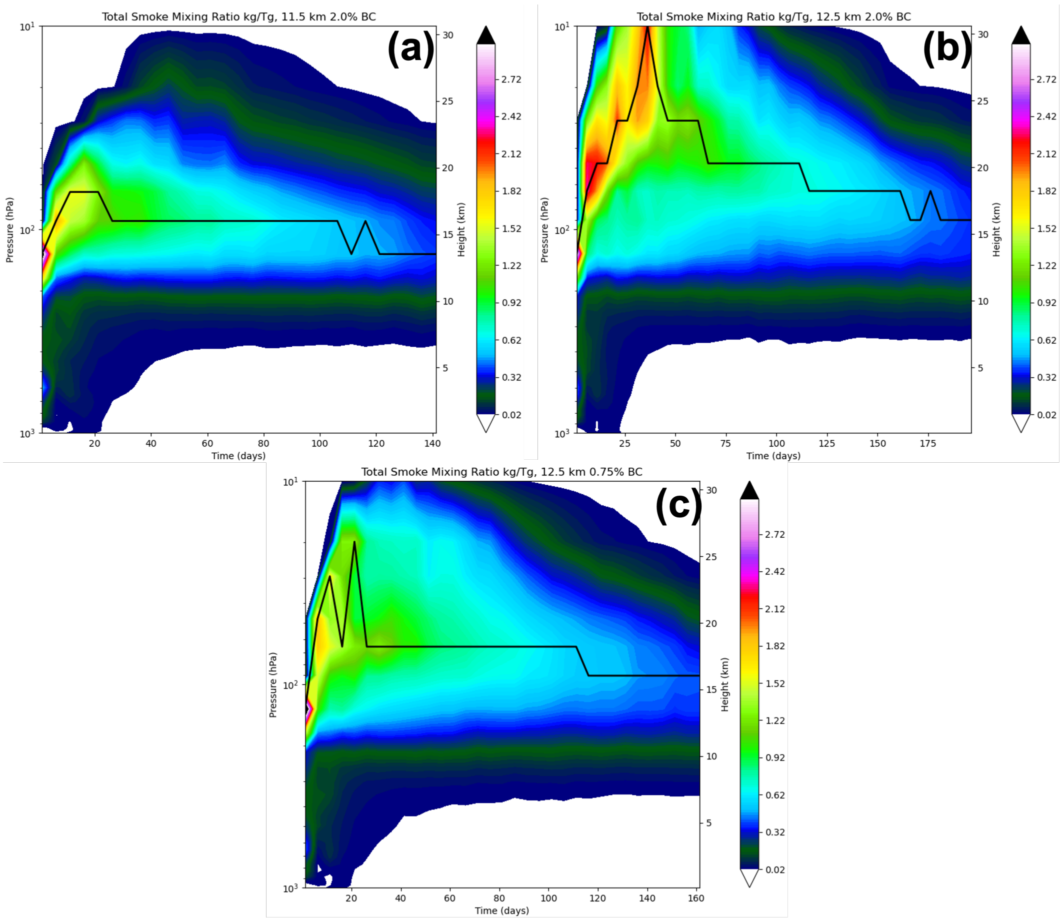

Figure 7: Horizontally averaged total smoke mixing ratio (kg/Tg) as a function of time and height for 0.25° grid spacing simulations with (a) 11.5 km injection height and 2.0% BC fraction, denoted "Perturb1" in Table 1, (b) 12.5 km injection height and 2.0% BC fraction, denoted "Perturb2" in Table 1 and (c) 12.5 km injection height and 0.75% BC fraction, one of the tests labeled "Perturb3" in Table 1. The black line in each figure denotes the center of mass of the smoke plume.

as well as other instrument effects. Nevertheless, the height metric from the simulations assists in tuning the simulations to observations.

Figure 7a shows results for an injection height of 11.5 km with 2.0% BC fraction, which produced a 4.4 month e-decay timescale, a bit too short relative to observations. It appears the height of the plume is too low with peak heights of around 18 km altitude. Figure 7b depicts the smoke evolution for an injection height of 12.5 km with 2.0% BC fraction. It is clear that the peak heights for this experiment are too high with values up to nearly 30 km altitude that stay elevated above 20 km altitude for several months. The e-decay timescale produced from this experiment is 6.3 months, which is too long relative to observations. Finally, Fig. 7c shows results for an injection height of 12.5 km only with 0.75% BC fraction. The plume height is more similar to observations than the other two sensitivity tests with values near 22 - 25 km altitude initially and then a steady value of $\sim$ 18 km that lasts several months. The e-decay timescale for this experiment is 5.1 months, which is also very similar to observations.

Table 1: Smoke plume and resolution settings for different model experiments. Note that the mass column refers to the injected stratospheric mass only. The “N” in “7kmN” refers to nonhydrostatic dynamics while all other grid spacings are run with hydrostatic.

Experiment	Injection Height	Mass	BC Fraction	Model Grid Spacing
Control	13.5 km	0.2 Tg	2%	2.0°/1.0°/0.25°/7km/7kmN
Perturb1	11.5 km	0.2 Tg	2%	0.25°
Perturb2	12.5 km	0.2 Tg	2%	0.25°
Perturb3	12.5 km	0.2 Tg	0.5%/0.75%	0.25°

Given that the best estimate for the observed injection height is $\sim$ 12 km and the model vertical resolution is only $\sim$ 1 km near the tropopause, we assess that the optimal BC fraction is $\sim$ 1%. This assessment is based on the simulation with a 12.5 km injection height and 0.75% BC fraction, which best matched observations. The optimal BC mass fraction of $\sim$ 1% is a 50% reduction from the control experiment as well as prior studies (e.g., Yu et al., 2019) and requires a numerically converged solution of $\sim$ 0.25° grid spacing. The final optimal smoke plume characteristics for the BC17 event determined from GEOS simulations are as follows: 0.2 Tg stratospheric smoke mass, 1% BC mass fraction, 300 - 350 nm particle radius and $\sim$ 12 km injection height. Table 2 lists the model resolution and optimal smoke plume characteristics determined from various studies of the BC17 event. This table serves as a quick reference for comparing the essential components of these studies and where the current study fits into the literature.

Lastly, all the simulations in this paper utilize externally mixed BC and observations suggest they are internally mixed (e.g., coated by OC). Coated particles have a specific light absorption mass cross section about two times larger than uncoated particles. Thus, internal mixing would need an even lower BC mass fraction in the optimal simulation to match the observed stratospheric lifetime and peak height (Lee et al., 2022).

Table 2: Model resolution and optimal settings for smoke plume characteristics for BC17 simulations determined from various papers. “Y19” is Yu et al. (2019), “C19” is Christian et al. (2019), “T20” is Torres et al. (2020), “D21” is Das et al. (2021), “D22” is D’Angelo et al. (2022) and “G22” is the current study. The mass column refers to the smoke mass placed at the injection height. All studies use a coupled model (between aerosols, radiation and dynamics) except that of “C19”.

Study	Model Grid Spacing	Injection Height	BC Fraction	Mass
Y19	1.9° x 2.5°	12 - 13 km	2%	0.3 Tg
C19	2.0° x 2.5°	13.7 km	6%	0.2 Tg
T20/D21	0.5°	10 - 12 km	2.5%	0.3 Tg
D22	1.0°, 1.9° x 2.5°	13.5 km	2%	0.2 Tg
G22	0.25°	12 km	1%	0.2 Tg

4 Vorticity Dynamics

Previous studies have documented the occurrence of long-lived, anti-cyclonic vortices associated with wildfire smoke plumes as they rise into the stratosphere and travel across the globe (Khaykin et al., 2020; Kablick et al., 2020; Lestrelin et al., 2021). The collocation of smoke plumes with a vorticity anomaly can enhance the concentration of smoke, which can lead to greater radiative absorption, self-lofting and longer stratospheric residence times. In this section, the vorticity dynamics of the smoke plumes in the GEOS simulations are analyzed to understand how these anomalies are initially formed and maintained.

While previous studies have relied on potential vorticity (PV) to study these features, we focus on the vorticity field for a couple of reasons. First, one of the primary motivations for analyzing PV is to track flow features through the PV conservation principle, which is only valid for frictionless, adiabatic motions. The smoke plumes, however, do not satisfy adiabatic motions due to significant radiative effects, especially during the early stages of the plume evolution. Thus, the conservation principle does not apply and other fields, such as the total smoke mixing ratio can be used to track the plumes. Second, the PV field does provide a more concise framework for interpreting the interplay between the dynamics and heating, which is useful. However, our goal here is to understand how the plume vortices are formed and maintained from fundamental variables and processes predicted or diagnosed from the numerical model, such as velocities and diabatic heating. The vorticity equation contains specific terms that allow for this type of attribution. The relative vorticity evolution equation in isobaric coordinates can be expressed as

$$\frac{D\zeta_p}{Dt} = -\left(\zeta_p + f\right)\left(\frac{\partial u}{\partial x} + \frac{\partial v}{\partial y}\right) - \frac{2\Omega cos\phi}{a}v + \left(\frac{\partial \omega}{\partial y}\frac{\partial u}{\partial p} - \frac{\partial \omega}{\partial x}\frac{\partial v}{\partial p}\right) + \mathbf{D}, \tag{4}$$

where ζ_p is the relative vertical vorticity on a surface of constant pressure, f is the Coriolis parameter, Ω is the angular frequency of the Earth, ϕ is the latitude, a is the radius of the Earth and ω is the vertical velocity in pressure coordinates ($\omega = Dp/Dt$). Following a parcel, the evolution of relative vorticity is controlled by the divergence of preexisting absolute vorticity (first term on the right-hand-side (RHS) of Eq. 4), the meridional change in Earth's rotation (beta term; second term on the RHS) and the tilting of horizontal components of vorticity into the vertical by variations in the vertical velocity (third term on the RHS). Finally, the **D** term represents sub-grid scale dissipation effects present in the model, which we assume to be small at the vertical levels analyzed here. This term is still useful to include in Eq. 4 for discussion purposes.

Figure 8 shows vertically averaged, horizontal cross sections of relative vorticity within the smoke plumes at 6.2 days into the simulations with various grid spacings. Vorticity in regions of total smoke mixing ratio greater than 10^{-9} kg/kg (or 1.0 kg/Tg) is averaged above 150 hPa to produce these plots. Each panel in Fig. 8 is approximately centered on the peak value of the total smoke mixing ratio to highlight the center of mass of the plumes. An anti-cyclonic vortex is present in the core of the plumes for each simulation as shown by the concentrated regions of negative vorticity. The peak values are around -3.5×10^{-5} s^{-1} in the 2.0° and 1.0° simulations $\sim$ -7.5×10^{-5} s^{-1} in the 0.25° simulation and $\sim$ -5.0×10^{-5} s^{-1} in the 7 km simulation. The vortex is significantly more diffuse and spread out in the 2.0° and 1.0° simulations as compared to the 0.25° and 7 km runs despite the fact that all simulations start with the same areal coverage of smoke. Figures 8c and 8d show that more positive vorticity begins to form and becomes entrained into the primary anti-cyclonic vortex in the higher resolution simulations. This is tied into the horizontal convergence and associated vertical transport, which is well resolved in the 0.25° and 7 km simulations as described in section 3.2.

At longer time periods into the simulations, the location and structure of the vortex is substantially different in each simulation. Figure 9 shows the same kind of plots as in Fig. 8, only at 41.2 days into the simulations. In the 2.0° run, the maximum in to-

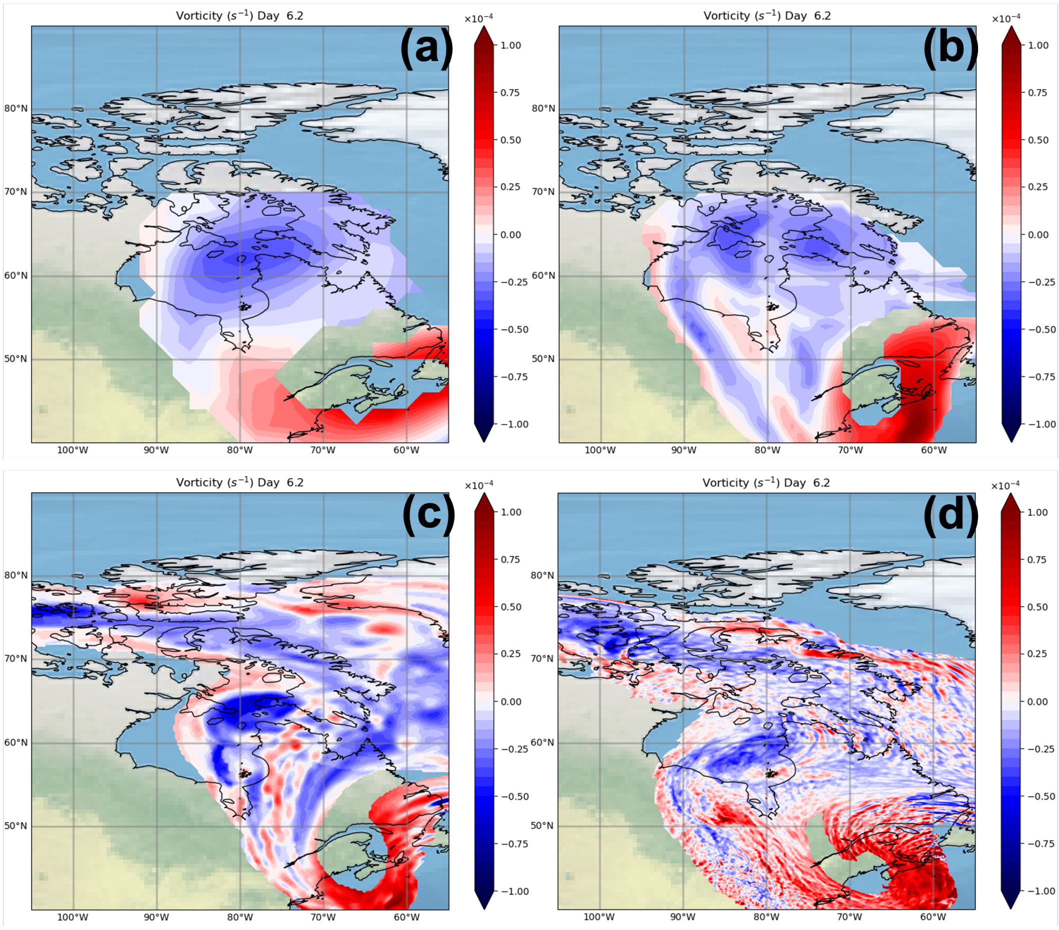

Figure 8: Vertically averaged, horizontal cross sections of vorticity in s^{-1} contained within the smoke plumes at 6.2 days into the simulations for grid spacings at (a) 2.0° (b) 1.0° (c) 0.25° and (d) 7 km. Vorticity in regions of total smoke mixing ratio greater than 10^{-9} kg/kg (or 1.0 kg/Tg) is averaged above 150 hPa to produce these plots.

tal smoke mixing ratio is very small (not shown) and the anti-cyclonic vortex has disappeared leaving a region of positive vorticity, which is likely the result of other synoptic scale features. In the 1.0° case, an anti-cyclonic vortex is still present at this time, but it is very weak and diffuse with peak values around -1.25$\times10^{-5}$ s^{-1} located over Ireland and the United Kingdom. The 0.25° simulation is still maintaining a coherent vortex located to the North of Alaska with peak values a bit larger than -2.5$\times10^{-5}$ s^{-1}. The main reason for the differences in location of the plumes is the height they attain, which results in transport differences from the environmental flows. The structure of the vortex and the ability to confine the smoke and assist in self-lofting is part of this process. In the 7 km simulation, the vortex is centered over Vancouver Island with similar peak values of vorticity as the 0.25° case. However, the 7 km run has much more small-scale variability in the vorticity field with many filaments of positive vorticity present in the core of the vortex, which could potentially weaken the integrated circulation through Stokes' theorem.

To understand how the anti-cyclonic vortex described above is formed, high frequency output from the 0.25° optimal simulation discussed in Section 3.3 is analyzed. Figure 10 depicts the background relative and absolute vorticity on August 12, 2017 at

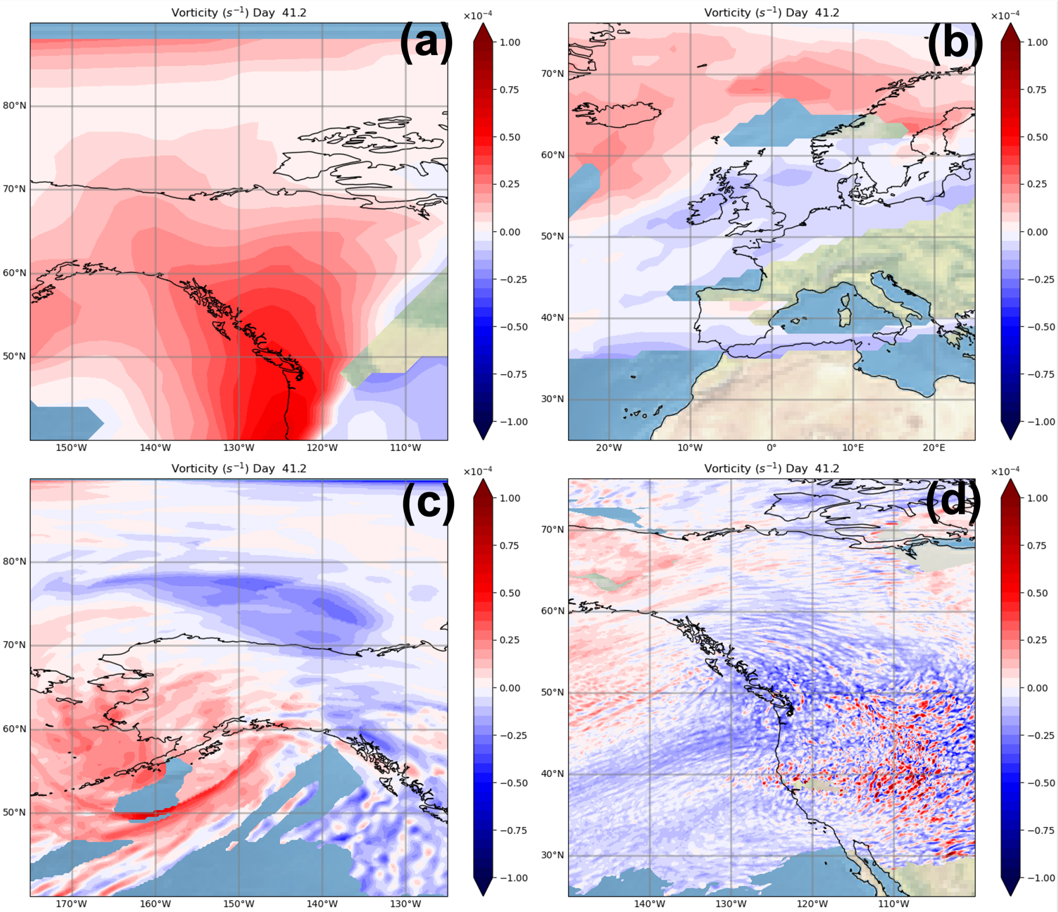

Figure 9: The same type of plot as in Fig. 8, only at 41.2 days into the simulations following the smoke plume.

1800 UTC in the region where the smoke plume is initialized and 1 h before the smoke injection begins. The plots in Fig. 10 are horizontal cross sections at 150 hPa, which is at or just above the injection height of 12.5 km. The relative vorticity in Fig. 10a shows a broad region of anti-cyclonic vorticity in the smoke plume area denoted on the figure. This region of anti-cyclonic relative vorticity is also present at 100 hPa (not shown), but some bands of cyclonic relative vorticity are present as well. The absolute vorticity in Fig. 10b is positive everywhere, including at higher altitudes, which indicates that the planetary vorticity dominates over the relative vorticity. At these high latitudes, the Coriolis parameter has values over 1×10^{-4} s^{-1}, which easily outweighs the relative vorticity in the stratosphere.

Figure 11 shows the divergence, tilting and material tendency terms from Eq. 4 along with the relative vorticity and divergence all located within the smoke plume at 0000 UTC August 13, which is the end of the 5 h smoke forcing period. These fields are shown at 150 hPa like those in Fig. 10. The beta term in Eq. 4 is about an order of magnitude smaller than the other terms and can be neglected. The first thing to note is that the smoke forcing quickly develops an anti-cyclonic relative vorticity anomaly (Fig. 11a) within the smoke plume with peak values of $\sim$ -7×10^{-5} s^{-1}, which is about a factor of three larger than the background values shown in Fig. 10a. Collocated with this relative vorticity anomaly is a positive divergence signature (Fig. 11b) indicating the air is

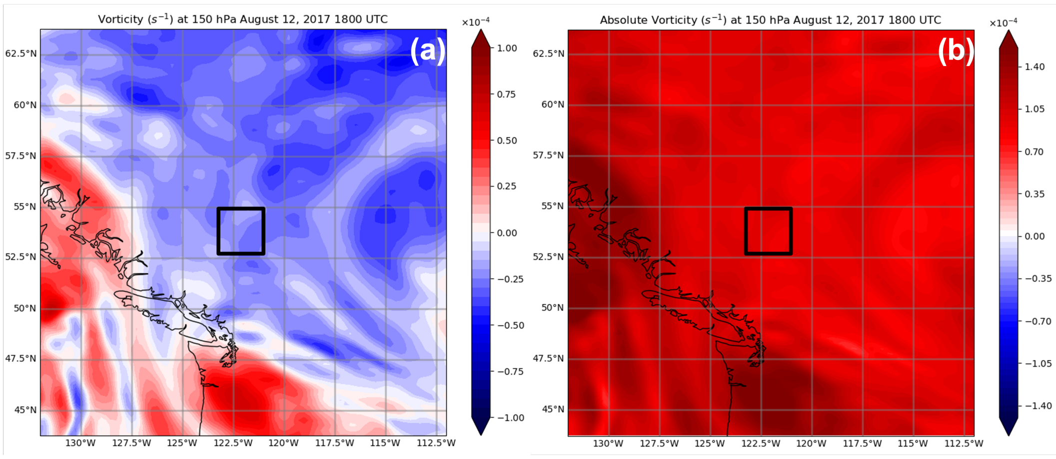

Figure 10: Horizontal cross sections of vorticity in s^{-1} on August 12, 2017 at 1800 UTC in the region where the smoke plume is initialized in the model. Panels (a) and (b) show relative vorticity and absolute vorticity, respectively, both at 150 hPa. The black box denotes the approximate region where the smoke plume is injected into the model. Note the slightly larger colorbar range in panel (b) compared to panel (a), which allows better visibility

spreading out at this level. The 150 hPa level is near the top of the smoke plume and there is also an updraft present at this height (not shown), which is consistent with diverging air at the top of the rising plume. Given that the absolute vorticity is positive everywhere (Fig. 10b), the diverging air is inducing a spin-down effect of the cyclonic absolute vorticity, which results in a negative divergence tendency (Fig. 11c). The divergence tendency values are much larger than those from the tilting tendency (Fig. 10d) at this time, so that the material tendency (Fig. 11e) is almost fully described by the divergence term. This material tendency increments the prior relative vorticity approximated by that shown in Fig. 10a to produce the current relative vorticity (Fig. 11a), which has a very similar structure to the material and divergence tendency terms.

Following the smoke plume in a Lagrangian frame of reference, Fig. 12 shows the same fields as in Fig. 11 only at 0000 UTC August 14, one day later. The fields are also shown at 150 hPa because this is where the peak smoke concentrations are located at this time. The smoke plume has grown significantly in size compared to the previous day and the relative vorticity field (Fig. 12a) shows a large region of anti-cyclonic vorticity with peak values concentrated in the plume core at or just above -1$\times10^{-4}$ s^{-1}. These values and those from other time periods show that the smoke plume vortex has a Rossby number $\leq$ 1. In the center of the plume, there is a strip of very low vorticity that separates the core of strong anti-cyclonic vorticity. This region is generally consistent with converging air (negative values of divergence in Fig. 12b), which acts to stretch the cyclonic absolute vorticity leading to a positive divergence tendency (Fig. 12c). Outside of this core region, diverging air (positive values of divergence in Fig. 12b) is leading to a negative divergence tendency (Fig. 12c) similar to that described above at 0000 UTC August 13. The divergence tendency continues to dominate over the tilting tendency (Fig. 12d) with the exception of a region on the western edge of the plume where the shear in the horizontal and vertical wind is largest. The material tendency shown in Fig. 12e reflects the divergence tendency very closely and the positive values in the center of the plume are responsible for the strip of very low vorticity observed in Fig. 12a. Smoke is present at higher altitudes (100 hPa) at this time period and the relative vorticity field at this level is compact and more uniform with positive divergence everywhere (not shown).

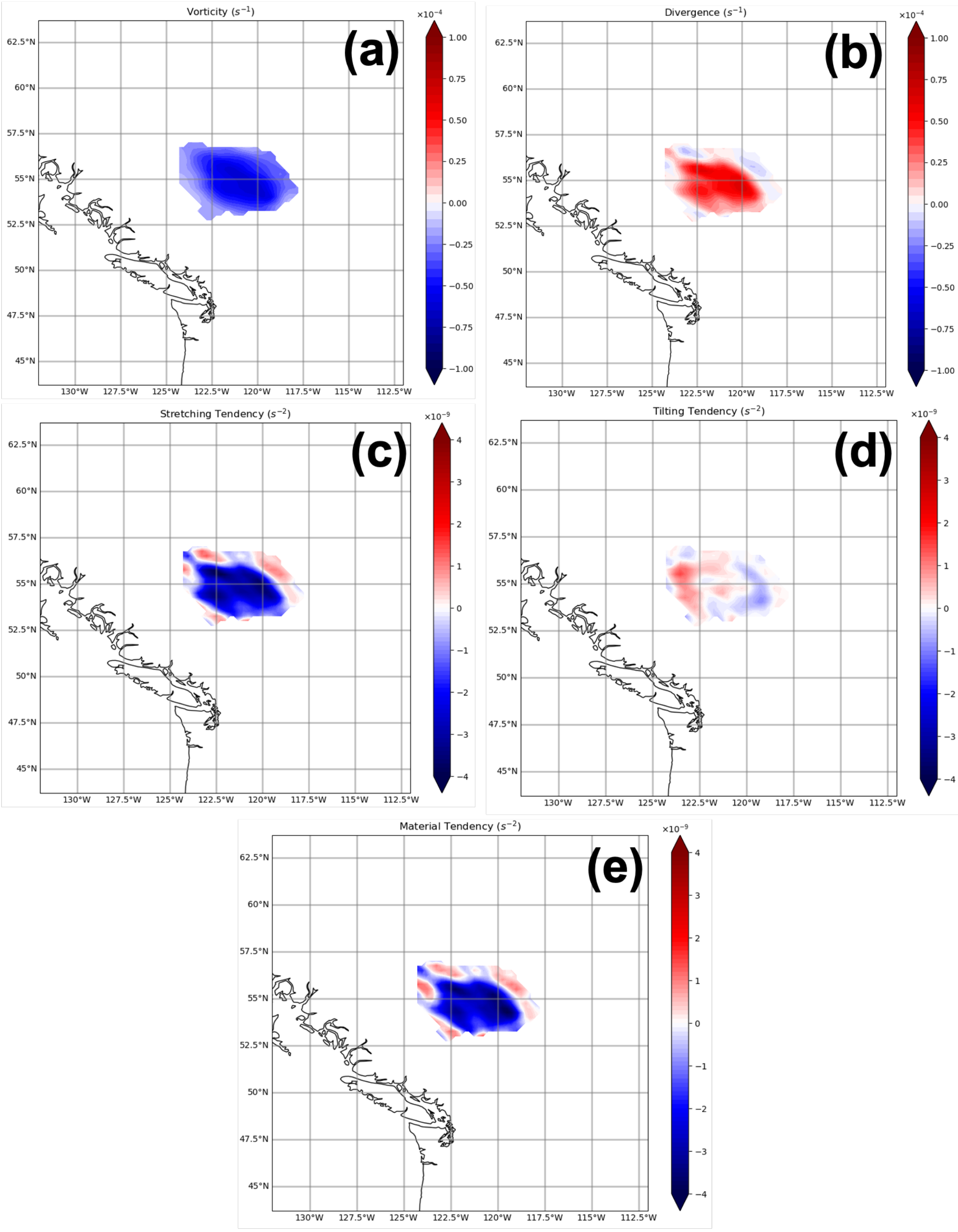

Figure 11: Horizontal cross sections at 150 hPa showing different fields relevant to the budget of relative vorticity within the smoke plume on August 13, 2017 at 0000 UTC. The fields are shown in regions of total smoke mixing ratio greater than 10^{-9} kg/kg (or 1.0 kg/Tg). Panels (a), (b), (c), (d) and (e) show relative vorticity (s^{-1}), divergence (s^{-1}), divergence tendency (s^{-2}), tilting tendency (s^{-2}) and the material tendency (s^{-2}), respectively.

This configuration is very similar to that shown in Fig. 11, which is also located at the top of the smoke plume.

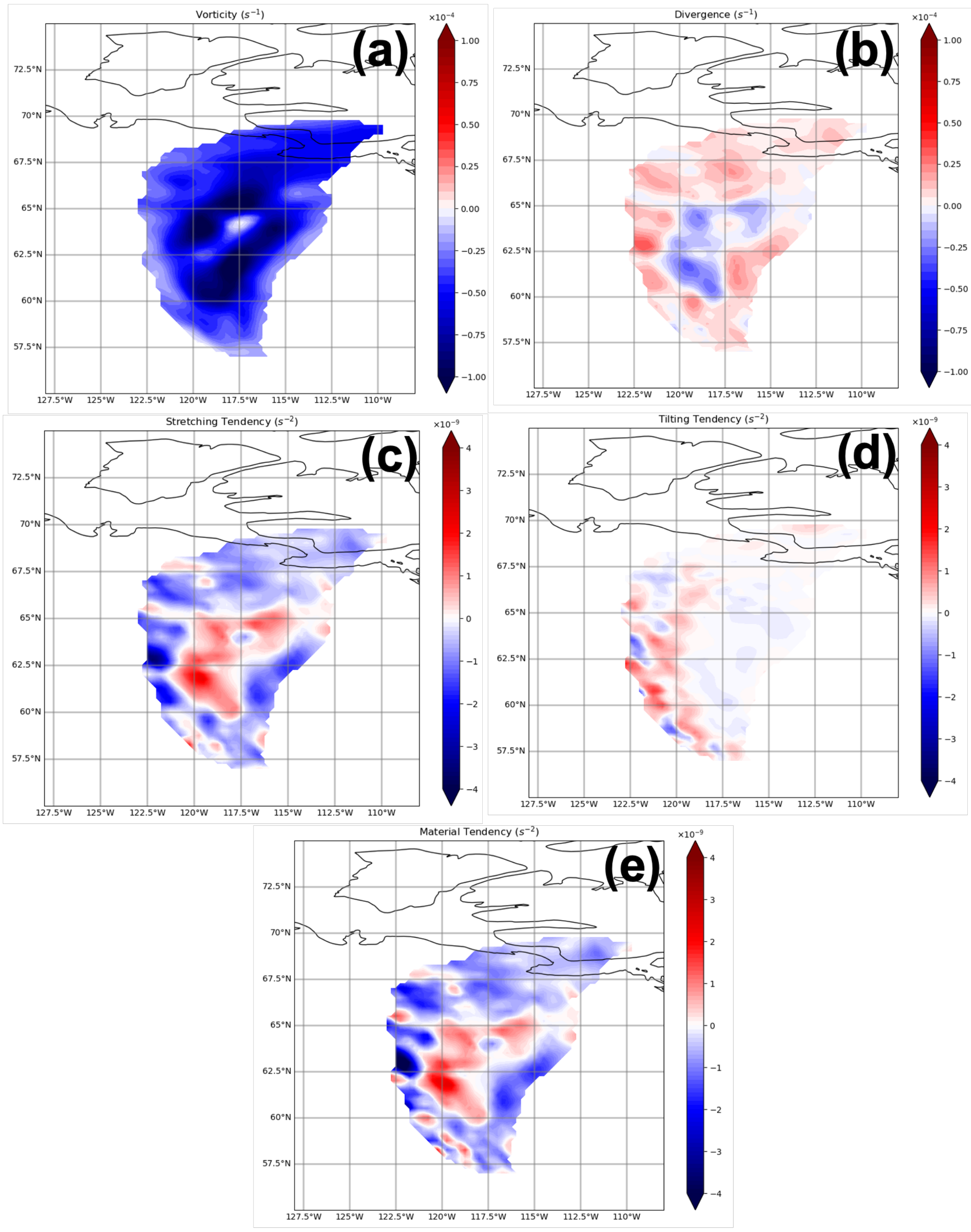

Figure 12: The same as in Fig. 11 only on August 14, 2017 at 0000 UTC. Panels (a), (b), (c), (d) and (e) show relative vorticity (s^{-1}), divergence (s^{-1}), divergence tendency (s^{-2}), tilting tendency (s^{-2}) and the material tendency (s^{-2}), respectively.

A Lagrangian conceptual model for the formation of smoke plume anti-cyclonic vortices emerges from these vorticity budget analyses. As the smoke plume absorbs solar radiation and begins to rise, the air diverges at the leading edge of the updraft, which induces a dilution of the cyclonic absolute vorticity (controlled by the sign of the Coriolis parameter). This dilution is a strong spin-down effect of the relative vorticity field, which dominates over all other terms, producing an anti-cyclonic vortex collocated with the smoke. The largest concentrations of smoke are present at these upper portions of the updraft. At levels below the leading edge, a combination of diverging and converging air associated with variability of the updraft is present that can perturb the structure of the vortex, but the anti-cyclonic tendency appears to be prominent.

Continuing to follow the smoke plume, Fig. 13 shows fields relevant to the vorticity budget at 0000 UTC September 3, which is $\sim$ 21 days after the smoke forcing. At this time period, the plume has reached equilibrium and ceased rising, as observed by the line tracing the center of mass in Fig. 7c. The height of the peak smoke mass is 20 hPa or $\sim$ 26 km, which is the level shown for the fields displayed in Fig. 13. The anti-cyclonic vortex is still compact and strong at this time period with peak relative vorticity values of $\sim$ -1$\times$10^{-4} s^{-1} in Fig. 13a. The divergence field (Fig. 13b) is weaker at this time period as the updraft has diminished and the plume has reached its peak height. Much of the divergence field in the plume is negative with a scattering of some positive regions, but when averaged over the plume, converging air is found. The dominance of converging air is more prominent at the top of the plume (10 hPa; not shown), which is consistent with a decaying updraft transitioning to a downdraft. The divergence tendency in Fig. 13c is dominated by positive values, which are driven by the concentration of cyclonic absolute vorticity from the converging air. The tilting tendency is negligible at this time period so the material tendency in Fig. 13d is fully described by the divergence effect, which is acting to destroy the anti-cyclonic vortex. This process is basically the exact opposite to how the anti-cyclonic vortex was formed as outlined above. Eventually, the vortex succumbs to this decay mechanism in addition to that from sub-grid scale dissipation processes as defined by the D term in Eq. 4.

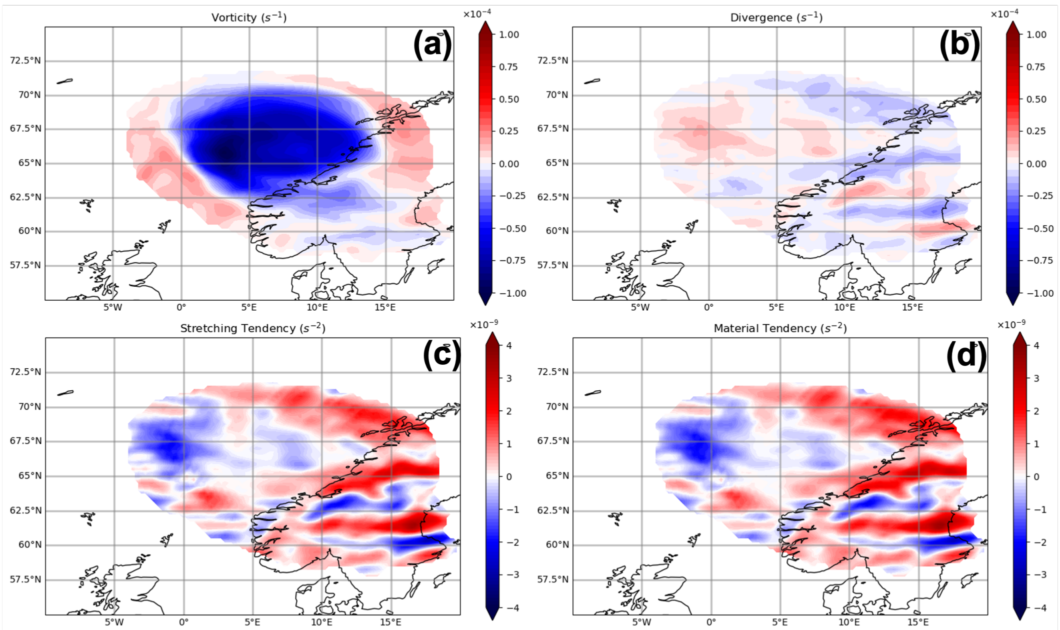

Figure 13: Horizontal cross sections at 20 hPa showing different fields relevant to the budget of relative vorticity within the smoke plume on September 3, 2017 at 0000 UTC. The fields are shown in regions of total smoke mixing ratio greater than 10^{-9} kg/kg (or 1.0 kg/Tg). Panels (a), (b), (c) and (d) show relative vorticity (s^{-1}), divergence (s^{-1}), divergence tendency (s^{-2}), and the material tendency (s^{-2}), respectively.

5 Summary and Conclusions

In this paper, the dynamics of wildfire smoke plumes and their dependence on specified smoke characteristics are examined in global climate simulations at a wide range of horizontal grid spacings (2.0°, 1.0°, 0.25°, 7 km and 7 km-nonhydrostatic). While the focus of the study is on the "megafire" event that occurred in British Columbia in August of 2017, the results and discussion are relevant to a much wider range of cases. The main goal of this work is to understand how the resolved energetics of the modeling system can affect the plume dynamics and retrieval of important plume properties such as the total smoke mass and BC fraction, which together determine the BC mass, as well as the height used to initialize the plume in climate models. Significant uncertainty is present in estimating these properties, which are determined either by analyzing satellite data (e.g., (Peterson et al., 2018)), which have several impactful assumptions, or by combining climate models with satellite data (e.g., (Yu et al., 2019)). Climate models are a powerful resource, but they have their own set of uncertainties, such as the treatment of the microphysical and optical properties of smoke particles, initial conditions and resolution limitations.

Many modeling studies are conducted with very coarse grid spacing (e.g., 1°, 2° and larger) with the smoke plume injected at one or maybe a few model grid points. Simulations of this type are shown here to be very dissipative, relative to a reference simulation at 7 km, in terms of horizontal kinetic energy spectra, stratospheric lifetime, peak plume height and vorticity characteristics. For example, the 2.0° simulation that initializes the smoke plume at one grid point underestimates the stratospheric lifetime by $\sim$ 50%, peak plume height by $\sim$ 40% and is missing a large chunk of kinetic energy and anti-cyclonic vorticity associated with the plume. In the 1.0° simulation that samples the plume with four grid points, the stratospheric lifetime and peak height are underestimated by $\sim$ 15% and 23%, respectively, with substantial kinetic energy missing and an anti-cyclonic vortex that is very weak and diffuse at longer time periods. The 0.25° simulation (64 grid points covering plume) produced only small errors in the lifetime ($\sim$ 4%) and peak height ($\sim$ 6%), which is consistent with well-resolved kinetic energy near the plume scale and a robust vortex. These results indicate that the 0.25° simulation has essentially reached convergence. As a result, in order to produce a dynamically accurate and well-resolved simulation, the smoke plume must be sampled by the model grid at $\sim$ 7 - 8 Δx. This "effective resolution" applies to the GEOS model studied here, but other global modeling systems produce similar results (e.g., (Skamarock et al., 2014)). A 7 km nonhydrostatic simulation was also conducted and compared to the 7 km hydrostatic experiment to examine the effects of the vertical inertial terms (and sub-grid diffusion) on the smoke stratospheric lifetime. The nonhydrostatic results show a slightly reduced stratospheric lifetime relative to the hydrostatic simulation, indicating that nonhydrostatic dynamics produces an overall dissipative effect on the plume vertical transport.

Given the above results, sensitivity tests were conducted with 0.25° spacing simulations to determine the optimal injection height of the plume and BC mass fraction using the stratospheric lifetime ($\sim$ 5 months) and to some extent peak heights ($\sim$ 22 km) (Peterson et al., 2018; Khaykin et al., 2018; Yu et al., 2019; Das et al., 2021) as the truth anchor points. These tests indicate that the optimal injection height and BC mass fraction is $\sim$ 12 km and $\sim$ 1%, respectively, assuming an external mixture. If the BC is coated or internally mixed, as suggested by field data (Lee et al., 2022), an even lower BC mass fraction will be needed to match the observed lifetime. The $\sim$ 12 km injection height is supported by satellite observations (Peterson et al., 2018) and previous modeling studies (Yu et al., 2019). The 1% BC mass fraction is a reduction of 50% from nominal values and is based on a nearly converged model solution that matches kinetic energy spectra from theory/observations and a 7 km reference simulation. Utilizing the same injection height, under-resolved simulations at 1.0° or 2.0° grid spacing would require a large and likely artificial increase in the BC fraction/mass to produce the same stratospheric lifetime as the well-resolved 0.25° simulation.

The vorticity dynamics of the smoke plumes is also analyzed to understand the mechanisms responsible for the formation and evolution of previously documented anti-cyclonic vortices (Khaykin et al., 2020; Kablick et al., 2020; Lestrelin et al., 2021), which are shown here to have peak values of relative, vertical vorticity around -2$\times10^{-4}$ s^{-1}. To provide this understanding a relative, vertical vorticity budget in a Lagrangian frame of reference, moving with the smoke plume center of mass, was conducted. The results show that the formation and evolution of the anti-cyclonic vortex is dominated by the divergence tendency with only a small contribution from the tilting tendency. Further analysis provides the following conceptual model for the formation and destruction of smoke plume anti-cyclonic vortices. As the plume rises from radiative heating, the air diverges at the top of the updraft where the largest concentrations of smoke are found. This divergence aloft induces a dilution of the background cyclonic absolute vorticity, which is dominated by the Coriolis parameter. This dilution is a strong spin-down or negative tendency on the relative vorticity field, which produces an anti-cyclonic vortex very quickly (5 h) after the initial injection of smoke. At later times into the simulation ($\sim$ 21 days) when the plume has reached an equilibrium height, the updraft has decayed and the air is largely converging aloft, which induces a concentration of the absolute vorticity field and a positive relative vorticity tendency that acts to destroy the anti-cyclonic vortex.

As described above, there are various sources of uncertainty that cloud the study of wildfire smoke plumes and their climate effects. The results described in this paper help to minimize the uncertainty stemming from the resolved energetics of the modeling system and illustrates how an under-resolved model configuration can affect the dynamics of the smoke plumes and the estimation of important plume properties.

Acknowledgments

Author Guimond thanks members of the NASA/GSFC Global Modeling and Assimilation Office (GMAO), especially Matt Thompson and Michael Manyin, for providing software support and answering questions on the GEOS modeling system. Discussions with Gennaro D'Angelo of the Los Alamos National Laboratory (LANL) is acknowledged. This work was funded by the LANL Laboratory Directed Research and Development (LDRD) program.

6 Data Availability Statement

The GEOS model code is available at `https://github.com/GEOS-ESM/GEOSgcm`. An overview of the GEOS modeling system, documentation and publications can be found at `https://gmao.gsfc.nasa.gov/GEOS_systems/`. The datasets needed to reproduce the core results of this paper can be found at the following link: `https://doi.org/10.5281/zenodo.7139799`

References

Chin, M., Ginoux, P., Kinne, S., Torres, O., Holben, B. N., Duncan, B. N., . . . Nakajima, T. (2002). Tropospheric aerosol optical thickness from the gocart model and comparisons with satellite and sun photometer measurements. *J. Atmos. Sci.*, *59*, 461–483.

Christian, K., Wang, J., Ge, C., Peterson, D., Hyer, E., Yorks, J., & McGill, M. (2019). Radiative forcing and stratospheric warming of pyrocumulonimbus smoke aerosols: First modeling results with multisensor (epic, calipso, and cats) views from space. *Geophysical Research Letters*, *46*(16), 10061-10071.

Retrieved from `https://agupubs.onlinelibrary.wiley.com/doi/abs/10.1029/2019GL082360` doi: https://doi.org/10.1029/2019GL082360

D'Angelo, G., Guimond, S., Reisner, J., Peterson, D., & Dubey, M. (2022). Contrasting stratospheric smoke mass and lifetime from 2017 canadian and 2019/2020 australian megafires: Global simulations and satellite observations. *Journal of Geophysical Research: Atmospheres*, *127*, 1-20. doi: https://doi.org/10.1029/2021JD036249

Das, S., Colarco, P. R., Oman, L. D., Taha, G., & Torres, O. (2021). The long-term transport and radiative impacts of the 2017 british columbia pyrocumulonimbus smoke aerosols in the stratosphere. *Atmospheric Chemistry and Physics*, *21*(15), 12069–12090. Retrieved from `https://acp.copernicus.org/articles/21/12069/2021/` doi: 10.5194/acp-21-12069-2021

Fromm, M. D., Bevilacqua, R., Servranckx, R., Rosen, J., Thayer, J. P., Herman, J., & Larko, D. (2005, April). Pyro-cumulonimbus injection of smoke to the stratosphere: Observations and impact of a super blowup in northwestern Canada on 3-4 August 1998. *Journal of Geophysical Research: Atmospheres*, *110*(D8), D08205. doi: 10.1029/2004JD005350

Jolly, W. M., Cochrane, M. A., Freeborn, P. H., Holden, Z. A., Brown, T. J., Williamson, G. J., & Bowman, D. M. J. S. (2015). Climate-induced variations in global wildfire danger from 1979 to 2013. *Nature Communications*, *6*(1), 7537. Retrieved from `https://doi.org/10.1038/ncomms8537` doi: 10.1038/ncomms8537

Kablick, G. P., Allen, D. R., Fromm, M. D., & Nedoluha, G. E. (2020, July). Australian PyroCb Smoke Generates Synoptic-Scale Stratospheric Anticyclones. *Geophysical Research Letters*, *47*(13), e88101. doi: 10.1029/2020GL088101

Khaykin, S., Legras, B., Bucci, S., Sellitto, P., Isaksen, L., Tencé, F., ... Godin-Beekmann, S. (2020). The 2019/20 australian wildfires generated a persistent smoke-charged vortex rising up to 35 km altitude. *Communications Earth & Environment*, *1*(1), 22. Retrieved from `https://doi.org/10.1038/s43247-020-00022-5` doi: 10.1038/s43247-020-00022-5

Khaykin, S. M., Godin-Beekmann, S., Hauchecorne, A., Pelon, J., Ravetta, F., & Keckhut, P. (2018). Stratospheric smoke with unprecedentedly high backscatter observed by lidars above southern france. *Geophysical Research Letters*, *45*(3), 1639-1646. Retrieved from `https://agupubs.onlinelibrary.wiley.com/doi/abs/10.1002/2017GL076763` doi: https://doi.org/10.1002/2017GL076763

Lee, J. E., Gorkowski, K., Meyer, A. G., Benedict, K. B., Aiken, A. C., & Dubey, M. K. (2022). Wildfire smoke demonstrates significant and predictable black carbon light absorption enhancements. *Geophysical Research Letters*, *49*(14). doi: 10.1029/2022GL099334

Lestrelin, H., Legras, B., Podglajen, A., & Salihoglu, M. (2021). Smoke-charged vortices in the stratosphere generated by wildfires and their behaviour in both hemispheres: comparing australia 2020 to canada 2017. *Atmospheric Chemistry and Physics*, *21*(9), 7113–7134. Retrieved from `https://acp.copernicus.org/articles/21/7113/2021/` doi: 10.5194/acp-21-7113-2021

Lin, S. (2004). A "vertically-lagrangian" finite-volume dynamical core for global atmospheric models. *Mon. Wea. Rev.*, *132*, 2293–2307.

Malone, R. C., Auer, L. H., Glatzmaier, G. A., Wood, M. C., & Toon, O. B. (1985, October). Influence of Solar Heating and Precipitation Scavenging on the Simulated Lifetime of Post–Nuclear War Smoke. *Science*, *230*(4723), 317-319. doi: 10.1126/science.230.4723.317

Molod, A., Takacs, L., Suarez, M., & Bacmeister, J. (2015). Development of the geos-5 atmospheric general circulation model: Evolution from merra to merra2. *Geosci. Model Dev.*, *8*, 1339–1356.

Nastrom, G., & Gage, K. (1985). A climatology of atmospheric wavenumber spectra of wind and temperature observed by commercial aircraft. *J. Atmos. Sci.*, *42*, 950–960.

Peterson, D. A., Campbell, J. R., Hyer, E. J., Fromm, M. D., Kablick, G. P., Cossuth, J. H., & DeLand, M. T. (2018). Wildfire-driven thunderstorms cause a volcano-like stratospheric injection of smoke. *npj Climate and Atmospheric Science*, *1*(1), 30. Retrieved from https://doi.org/10.1038/s41612-018-0039-3 doi: 10.1038/s41612-018-0039-3

Peterson, D. A., Fromm, M. D., McRae, R. H. D., Campbell, J. R., Hyer, E. J., Taha, G., ... DeLand, M. T. (2021). Australia's black summer pyrocumulonimbus super outbreak reveals potential for increasingly extreme stratospheric smoke events. *npj Climate and Atmospheric Science*, *4*(1), 38. Retrieved from https://doi.org/10.1038/s41612-021-00192-9 doi: 10.1038/s41612-021-00192-9

Rienecker, M. M., Suarez, M. J., Todling, R., Bacmeister, J., Takacs, L., Liu, H.-C., ... Nielsen, J. (2008). *The geos-5 data assimilation system - documentation of versions 5.0.1, 5.1.0, and 5.2.0* (Tech. Rep. No. 27). Greenbelt, MD, USA: NASA Goddard Space Flight Center.

Skamarock, W., Park, S.-H., Klemp, J. B., & Snyder, C. (2014). Atmospheric kinetic energy spectra from global high-resolution nonhydrostatic simulations. *J. Atmos. Sci.*, *71*, 4369-4381.

Torres, O., Bhartia, P. K., Taha, G., Jethva, H., Das, S., Colarco, P., ... Ahn, C. (2020, May). Stratospheric Injection of Massive Smoke Plume From Canadian Boreal Fires in 2017 as Seen by DSCOVR-EPIC, CALIOP, and OMPS-LP Observations. *Journal of Geophysical Research (Atmospheres)*, *125*(10), e32579. doi: 10.1029/2020JD032579

Wang, J., Park, S., Zeng, J., Ge, C., Yang, K., Carn, S., ... Omar, A. H. (2013, February). Modeling of 2008 Kasatochi volcanic sulfate direct radiative forcing: assimilation of OMI SO_2 plume height data and comparison with MODIS and CALIOP observations. *Atmospheric Chemistry & Physics*, *13*(4), 1895-1912. doi: 10.5194/acp-13-1895-2013

Weisman, M. L., Skamarock, W. C., & Klemp, J. B. (1997). The resolution dependence of explicitly modeled convective systems. *Mon. Wea. Rev.*, *125*, 527.

Wikipedia contributors. (2022). *Megafire — Wikipedia, the free encyclopedia.* Retrieved from https://en.wikipedia.org/w/index.php?title=Megafire&oldid=1086807350 ([Online; accessed 13-June-2022])

Yu, P., Toon, O. B., Bardeen, C. G., Zhu, Y., Rosenlof, K. H., Portmann, R. W., ... Robock, A. (2019). Black carbon lofts wildfire smoke high into the stratosphere to form a persistent plume. *Science*, *365*(6453), 587–590. Retrieved from https://science.sciencemag.org/content/365/6453/587 doi: 10.1126/science.aax1748